

# Mapping of temperature and CO<sub>2</sub> column density in a standard flame by multispectral imaging

Juan Meléndez, Javier Talavante, Guillermo Guarnizo and Fernando López

LIR - Infrared Laboratory, Department of Physics  
Universidad Carlos III de Madrid, 28911 Leganés, Spain

## ABSTRACT

Temperature measurement in flames is a challenging problem. Recently, hyperspectral imaging has demonstrated to be able to provide accurate temperature maps in a standard flame. However, hyperspectral imagers are expensive instruments, and the data analysis is laborious. Thus, a more simple approach to temperature imaging would be advisable. Since important and systematic differences exist in the low-resolution spectra of flames as a function of their temperature and chemical composition, it is in principle possible to retrieve these parameters by means of multispectral imaging. In this work, a standard flame, whose temperature and CO<sub>2</sub> concentration are known, is studied with an infrared camera in the MIR band (3 to 5  $\mu\text{m}$ ), provided with a six interference filter wheel. High-resolution emission spectra are calculated, using the HITEMP2010 database, as a function of flame temperature (T) and CO<sub>2</sub> column density ( $Q_{\text{CO}_2}$ , measured in ppm·m), and integrated over the spectral transmittance profile of the selected interference filters. Measured radiances in each channel are compared to these simulated values and the absolute error is minimized at each pixel to retrieve values of T and Q, obtaining temperature and column density maps for the flame. Results are compared to the known values of the standard flame. First estimations of errors are found to be  $\Delta T < 100$  K and  $\Delta Q_{\text{CO}_2} < 400$  ppm·m for flames with  $T \sim 2200$  K and  $Q_{\text{CO}_2} \sim 3500$  ppm·m. The possibility of reducing the number of filters and their effect on accuracy is studied.

**Keywords:** Infrared imaging, Multispectral and hyperspectral imaging, Remote sensing and sensors, Spectroscopy, Image processing, Combustion diagnostics, Temperature measurement.

## 1. INTRODUCTION

The optimization of a vast number of industrial processes is directly linked to accurate control of their temperatures. Appropriate monitoring improves consistency and energy efficiency in manufacturing processes, reduces wastage and pollution, increases reliability, and extends intervals of maintenance tasks. In particular, accurate temperature measurement in combustion and flame processes is of paramount importance, but it is also a challenging problem, due to the harsh environment and the alteration that intrusive probes (i.e., thermocouples) induce in the flame. Thus, the state-of-the-art techniques are those of optical thermometry, such as CARS (Coherent Anti-Stokes Raman Spectroscopy), DFWM (Degenerate Four-Wave Mixing), LIGS (Laser Induced Grating Spectroscopy), or luminescence of thermographic phosphors. All these techniques involve the use of a laser and require instrumentation that is complex to install and operate outside the laboratory. Still, their uncertainty is relatively high: generally not better than 5 % of the temperature in kelvin.<sup>1</sup>

In order to address this metrological challenge, the EMPRESS project,<sup>1</sup> funded by the European Metrology Programme for Innovation and Research (EMPIR) proposed as one of its objectives to reduce the uncertainty of optical combustion thermometry by developing and characterizing a portable standard flame with known and reproducible temperature, traceable to the International Temperature Scale of 1990 (ITS-90). This flame was developed by the British National Physical Laboratory (NPL), and measurements of temperature performed on it by infrared (IR) emission spectroscopy have demonstrated an accuracy of  $\sim 1\%$ , as reported in Sutton et. al.<sup>2</sup>

Measurements by emission spectroscopy are possible because emission/absorption lines have a well-known dependence on temperature. Therefore, the measured intensities of those lines can be fitted by a simulated spectrum built with a radiative model that uses the spectroscopic parameters of the gases in the flame (in particular, CO<sub>2</sub> and H<sub>2</sub>O): an algorithm changes iteratively temperature (T, measured in K) and column density

(concentration times optical path,  $Q$  measured in ppm·m) in the model until an optimal agreement is found, therefore retrieving values for  $T$  and  $Q$  in the flame.

This approach requires high-resolution spectra to fit the individual lines, and results reported in Sutton et al.<sup>2</sup> have been obtained with a hyperspectral imaging system,<sup>3</sup> that provides a spectral resolution of  $0.5 \text{ cm}^{-1}$ . Although the setup is straightforward and can be used outside the laboratory, the practical application of such a scheme to industrial settings finds difficulties both in the acquisition of data (since hyperspectral imagers are expensive instruments and image acquisition is slow) and in their analysis (because correct simulation of spectra is not easy, and iterative fitting of high-resolution spectra over an image is computationally demanding). A cheaper, faster, and less complex approach is needed to achieve practical temperature imaging of flames, which can be implemented on-site in industrial environments outside the laboratory and yet retain a good accuracy. This is one of the aims of the EMPRESS 2 project,<sup>4</sup> funded also by EURAMET (European Association of National Metrology Institutes).

The approach that will be proposed in this work is based on the fact that important and systematic differences exist in the low-resolution emission spectra of flames as a function of their temperature and chemical composition. Thus, in principle, it should not be necessary to resolve individual lines to estimate these parameters. This opens up the possibility of imaging temperature and column densities of chemical species in a flame with a multispectral system. The aim of this paper is to study that possibility, first from a theoretical point of view and then experimentally, with multispectral measurements of the portable standard flame of NPL.

In the following, Section 2 reviews the basic principles on which high- and low-resolution simulated emission spectra of a gas can be generated, as a function of temperature and concentration of chemical species, and explains the method proposed to retrieve temperature and column density from multispectral measurements. Section 3 describes the multispectral system used and its calibration. The feasibility of the proposed approach is assessed in Section 4 by estimating the expected error in  $T$  and  $Q$  due to uncertainty in measured radiance, whereas Section 5 describes the experimental measurements and results. Finally, Section 6 summarizes the results, draws conclusions, and suggests further work.

## 2. RADIATIVE MODEL AND RETRIEVAL METHOD

### 2.1 Radiative model

The spectral radiance ( $\mathcal{L}$ , measured in  $\text{W}/\text{m}^2 \cdot \text{sr} \cdot \text{cm}^{-1}$ ) emitted by any physical body at temperature  $T$  is given by

$$\mathcal{L}_{out}(\nu, T) = \mathcal{L}_{BB}(T, \nu) \cdot \varepsilon(T, \nu) \quad (1)$$

where  $\mathcal{L}_{BB}$  is the well-known blackbody emission, given by Planck's law, and  $\varepsilon(T, \nu)$  is emissivity, a dimensionless parameter ( $0 \leq \varepsilon \leq 1$ ) specific of the body. In conditions of local thermal equilibrium, Kirchhoff's law guarantees that absorptance,  $\alpha$ , i.e., the fraction of the incident radiation absorbed by a body, equals emissivity:  $\alpha(\nu) = \varepsilon(\nu)$ . Conservation of energy implies that  $\alpha + \tau + \rho = 1$ , where  $\tau$  is the transmitted fraction of radiation and  $\rho$  is the reflected fraction. For a gas,  $\rho = 0$  and thus

$$\varepsilon(\nu) = 1 - \tau(\nu) \quad (2)$$

On the other hand, Lambert-Beer's law specifies that transmittance in a gas or liquid can be written as

$$\tau(\nu, C, L, T) = e^{-a(\nu, T)CL} \equiv e^{-a(\nu, T)Q} \quad (3)$$

where  $a$  is the absorptivity,  $L$  is the optical path traveled in the gas by the radiation,  $C$  is the concentration (generally measured in parts per million, ppm),  $Q = CL$  is the column density (ppm·m), and the dependence of  $a$  on wavenumber and temperature has been shown explicitly. If there are more than one absorbing species,  $\tau(\nu)$  is just a product of terms like eq. (3), one for each species; if the concentration is not homogeneous, the product  $aCL$  is replaced by an integral.

Since absorptivities are well-known parameters that can be extracted from spectroscopic databases, a transmittance measurement over a spectral range provides, in principle, an accurate way to identify gases in a sample

and to determine their concentrations. This is the basis of classical IR absorption spectroscopy, but because of the direct relationship between  $\varepsilon$  and  $\tau$  (eq.2), it is also the basis of emission spectroscopy in flames, if a few basic assumptions are made:

- The flame is in local thermal equilibrium, so that Kirchhoff's law holds.
- The background is much colder than the flame and its emission can be neglected.
- Since we are going to operate in the mid-IR region, the effects of scattering can be neglected (because the typical size of particulate matter in a flame is much smaller than the wavelengths of mid-IR).

It will be assumed also, for simplicity, that both T and Q for each species are homogeneous along the optical path that corresponds to the field of view of each pixel (iFOV). This is obviously an approximation, and the retrieved values of T and Q should be considered as line-of-sight effective averages.

With these assumptions, the spectral radiance that enters in a camera or spectrometer that images the flame can be written as

$$\mathcal{L}_{in}(\nu, T, Q) = \mathcal{L}_{out}(\nu, T) \cdot \tau_{atm}(\nu) = \mathcal{L}_{BB}(T, \nu) \cdot (1 - e^{-a(\nu, T)Q}) \cdot \tau_{atm}(\nu) \quad (4)$$

where the emitted radiance of eq. (1) has been multiplied by the atmospheric transmittance  $\tau_{atm}(\nu)$  and eq. (2) and (3) have been used. In this work we will focus on the spectral region between 2000 and 2400  $\text{cm}^{-1}$ , where water vapor emission is negligible, and a complete combustion will be assumed, so that CO can be neglected also; in these conditions, the only contribution to flame emission is due to  $\text{CO}_2$ ; in the following, the column density of  $\text{CO}_2$  will be written simply as Q.

## 2.2 Retrieval method

It is clear that  $\mathcal{L}_{in}$  has a strong dependence on T because of the blackbody factor  $\mathcal{L}_{BB}$ . This dependence is simple and perfectly known for  $\mathcal{L}_{BB}$ , but it gets complicated for  $\mathcal{L}_{in}$  because the absorption/emission cross sections, and consequently the spectral absorptivities  $a(\nu)$ , depend also on T in a nontrivial way. Therefore, although in principle eq. (4) could be solved for T and Q if  $\mathcal{L}_{in}$  is measured over a certain spectral range, that strategy is not feasible in practice. Instead, a different approach is taken: absorptivities are obtained from the HITEMP2010<sup>5</sup> database so that simulated spectra can be generated, over the spectral range of interest, for any (T,Q) values. The process is iterated and the retrieved (T,Q) values are those that provide an optimal agreement between simulation and experimental spectrum.<sup>2</sup>

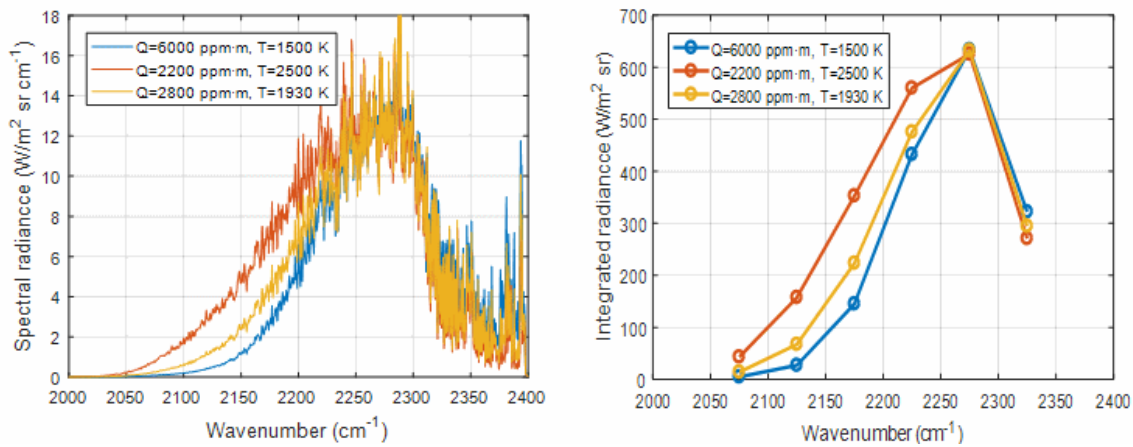


Figure 1: Left: Three simulated emission spectra for different column densities of  $\text{CO}_2$  and flame temperatures. Right: Integrated radiance over bands of  $50 \text{ cm}^{-1}$  width for the same high-resolution spectra of the left.

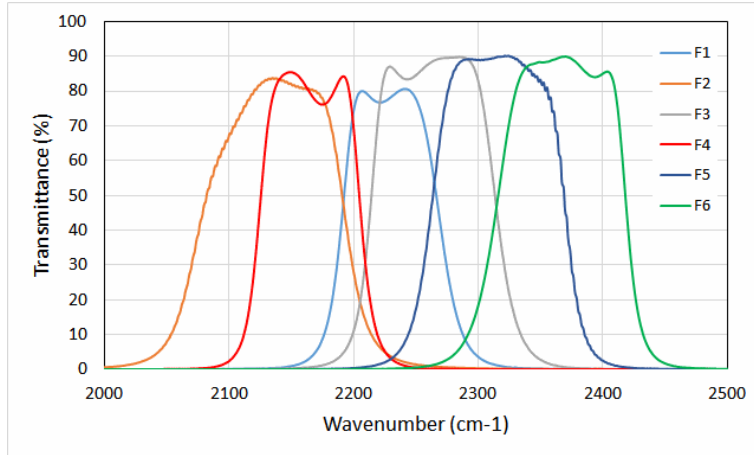


Figure 2: Transmittance profiles of the six interference filters used.

The strategy explained so far is based on fitting individual lines and thus needs high-resolution spectra. However, lines are grouped into ro-vibrational bands, and when the individual intensity of the lines changes because of temperature, the overall shape and intensity of the band also change. As a rule, as  $T$  increases the emitted radiance in each line increases, as expected from (4), but the effect is stronger for lines far from the band center because higher energy rotational levels become more populated. This means that at higher temperatures the band becomes wider. This effect can be seen in the left-hand side of Figure 1, which shows calculated spectra (using HITEMP2010 parameters) for three different temperatures and column densities of  $\text{CO}_2$ . The higher temperatures have smaller concentrations, so that emitted radiance at the maximum is very similar in all cases. However, increasing  $T$  means that the band grows wider, and the signal increases for wavenumbers far from the maximum. The sharp decrease for  $\nu \gtrsim 2300 \text{ cm}^{-1}$  is due to absorption by atmospheric  $\text{CO}_2$  that, being cold, takes place over a relatively narrow spectral region.

If the high-resolution spectra at the left-hand side of Figure 1 are integrated over spectral intervals of equal width ( $50 \text{ cm}^{-1}$  in this case), the result is a simulation of a multispectral measurement, as shown in the right-hand side. It is clear that a measurement system with a single band centered at  $2275 \text{ cm}^{-1}$  would be unable to distinguish between the three cases of the figure, but the ambiguity can be resolved using the information of additional bands. Therefore, retrieval of  $(T, Q)$  from the multispectral measurement can be made, in principle, as in the hyperspectral case, by iterative fitting of the experimental data with the simulation, which includes now an integration over the spectral band of the filter. The practical procedure is discussed further in the following section.

### 3. MULTISPECTRAL SYSTEM

The experimental measurements in this work have been performed using a Thermosensorik SME 640 camera as a multispectral system. It operates in the MIR band ( $3$  to  $5 \mu\text{m}$ ) and has an InSb Stirling-cooled FPA detector, with  $640 \times 512$  pixels. It features a rotating filter wheel placed immediately after the optics, where up to six interference filters of one-inch diameter can be placed. The spectral transmittance profiles of the filters used are shown in Figure 2. For each filter, a different integration time was used in order not to saturate the camera response, and a radiometric calibration was performed with a  $15 \times 15 \text{ cm}$  extended area blackbody radiator (model 4006G from Santa Barbara Infrared, Inc.) with a nominal emissivity of 0.9.

In order to radiometrically calibrate the multispectral system, a nominal spectral width  $\Delta_i$  is defined for each filter as the full width at half maximum (FWHM) of its spectral transmittance. The blackbody radiator is set at different temperatures and the measured digital number ( $\text{DN}_i$ ) is plotted versus the emitted radiance, integrated over  $\Delta_i$ . A least-square linear fitting provides the parameters  $\text{Gain}_i$  (slope) and  $\text{Offset}_i$  (y-intercept).

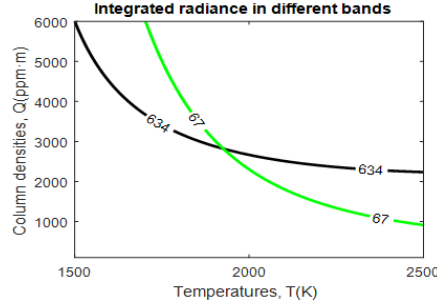


Figure 3: Couples of (T,Q) for CO<sub>2</sub> that provide the same values of emitted radiance in two bands. Green, 67 W/m<sup>2</sup>·sr between 2100 and 2150 cm<sup>-1</sup>; black, 634 W/m<sup>2</sup>·sr between 2250 and 2300 cm<sup>-1</sup>. These are the values of the yellow line in Figure 1 left. The point where the two lines cross is T=1930 K, Q=2800 ppm·m, the (T,Q) values of the yellow spectrum.

The measured radiance in the  $i$ -th channel can be subsequently obtained as

$$\mathcal{L}_i = \frac{\text{DN}_i - \text{Offset}_i}{\text{Gain}_i} \quad (5)$$

It must be pointed out that if the camera is not close enough to the blackbody during calibration, the effect of atmospheric absorption must be taken into account multiplying the emitted radiance by the average transmittance over the spectral interval  $\Delta_i$ .

When a multispectral measurement has been made, eq. (5) provides a *measurement vector*  $(\mathcal{L}_1, \dots, \mathcal{L}_6)$  with the radiometric information. Values of  $\mathcal{L}_i$  do not depend on the transmittance of the filter, since calibration is made against the total integrated radiance over the spectral width  $\Delta_i$ , but they do depend strongly on its spectral width. Therefore, it is convenient to divide  $\mathcal{L}_i$  by  $\Delta_i$ , to have an estimation of the spectral radiance at each filter central wavenumber. The normalized measurement vector  $(\frac{\mathcal{L}_1}{\Delta_1}, \dots, \frac{\mathcal{L}_6}{\Delta_6})$  may be considered as a low-resolution approximation to the real emission spectrum as measured at the location of the camera.

## 4. ERROR ESTIMATION

Before using the multispectral system to retrieve temperatures, it is useful to have an estimation of the expected error to assess if the approach is feasible.

### 4.1 Graphical method

Since the shape and intensity of the emission band depend on Q as well as on T, both parameters will have to be retrieved simultaneously. In fact, for any reasonable value of integrated radiance in a specific band, there is a one-dimensional continuum of (T,Q) couples that provides it. In a graph with T and Q axes, those couples form an *iso-radiance line*, as the black line in Figure 3, that corresponds to the 634 W/m<sup>2</sup>·sr measured between 2250 and 2300 cm<sup>-1</sup> in the right-hand side of Figure 1. If the line for another band is plotted, as the green line that corresponds to 67 W/m<sup>2</sup>·sr between 2100 and 2150 cm<sup>-1</sup>, they will intersect at the (T,Q) values of the flame. Since different filters have different iso-radiance lines, they will intersect, and therefore any two different filters will permit, in principle, to retrieve the (T,Q) values.

However, in a real measurement the effect of errors may be very important, depending on the filters. A graph of iso-radiance lines makes it possible to estimate the expected error for T and Q due to uncertainty in the radiance measured in each channel,  $\Delta\mathcal{L}_i$ , since the four curves defined by  $\mathcal{L}_i \pm \Delta\mathcal{L}_i$  for both filters delimit the region of T-Q values compatible with the measurement. Figure 4 shows two such graphs for two different pairs of filters. The area enclosed by the four curves is clearly much larger for the F5-F6 pair of filters than for the F2-F3 pair, so the (T, Q) values retrieved using F5 and F6 will be less reliable than those retrieved using F2 and F3.

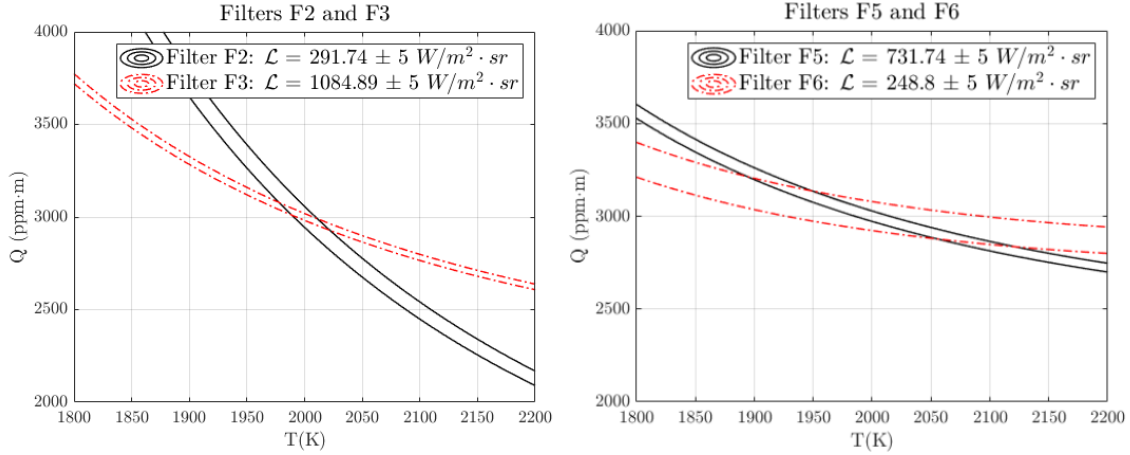


Figure 4: Iso-radiance lines in the  $Q$  vs.  $T$  graph for two different couples of filters. For the same uncertainty in radiance, errors in retrieved  $Q$  and  $T$  will be much smaller for filters (2,3), whose transmittance profiles are more separated than those of filters (5,6).

This difference is mainly due to two reasons. On the one hand, the curves for F2 and F3 intersect at a greater angle than those for F5 and F6. This means that they share less spectral information, which improves the estimation. The result is expected from the transmittance of the filters, since the passbands of F5 and F6 share a region of the spectrum, unlike those of F2 and F3, that hardly overlap. On the other hand, the regions between the two iso-radiance lines of the same filter are narrower in the case of F2-F3 than in F5-F6, for the same  $\Delta\mathcal{L}$ . This means that the spectral region of filters F2-F3 is more sensitive to variations in  $T$  and  $Q$  than that of F5-F6, which is to be expected given the emission spectra of Figure 1.

## 4.2 Montecarlo method

The graphic method just exposed is useful to understand the factors that influence errors in the retrieved values of  $T$  and  $Q$  and to get a rough estimation of them. For the purpose of obtaining a quantitative value, the Montecarlo method has been used. A normal error distribution with standard deviation  $\Delta\mathcal{L}_i$  has been created for each  $\mathcal{L}_i$ , considered as independent. The values of  $T$  and  $Q$  retrieved with these distributions have standard deviations  $\Delta T$  and  $\Delta Q$  whose values have been taken as the uncertainties of  $T$  and  $Q$  respectively.

Values of  $\Delta T$ ,  $\Delta Q$  are related to  $\Delta\mathcal{L}_i$  by the usual equations of uncertainty propagation:

$$\begin{aligned}\Delta\mathcal{L}_1 &= \frac{\partial\mathcal{L}_1}{\partial T} \cdot \Delta T + \frac{\partial\mathcal{L}_1}{\partial Q} \cdot \Delta Q \equiv \partial_T\mathcal{L}_1 \cdot \Delta T + \partial_Q\mathcal{L}_1 \cdot \Delta Q \\ \Delta\mathcal{L}_2 &= \frac{\partial\mathcal{L}_2}{\partial T} \cdot \Delta T + \frac{\partial\mathcal{L}_2}{\partial Q} \cdot \Delta Q \equiv \partial_T\mathcal{L}_2 \cdot \Delta T + \partial_Q\mathcal{L}_2 \cdot \Delta Q\end{aligned}\quad (6)$$

Where  $\partial_T\mathcal{L}_i \equiv \frac{\partial\mathcal{L}_i}{\partial T}$  and  $\partial_Q\mathcal{L}_i \equiv \frac{\partial\mathcal{L}_i}{\partial Q}$  are obtained numerically from the simulated emission spectra and are functions of  $T$  and  $Q$ . Solving for  $\Delta T$ ,  $\Delta Q$ :

$$\begin{aligned}\Delta Q &= \frac{\partial_T\mathcal{L}_1 \cdot \Delta\mathcal{L}_2 - \partial_T\mathcal{L}_2 \cdot \Delta\mathcal{L}_1}{\partial_T\mathcal{L}_1 \cdot \partial_Q\mathcal{L}_2 - \partial_T\mathcal{L}_2 \cdot \partial_Q\mathcal{L}_1} \\ \Delta T &= -\frac{\partial_Q\mathcal{L}_1 \cdot \Delta\mathcal{L}_2 - \partial_Q\mathcal{L}_2 \cdot \Delta\mathcal{L}_1}{\partial_T\mathcal{L}_1 \cdot \partial_Q\mathcal{L}_2 - \partial_T\mathcal{L}_2 \cdot \partial_Q\mathcal{L}_1}\end{aligned}\quad (7)$$

In order to ascribe values to  $\Delta\mathcal{L}_i$ , a sequence of images has been acquired of the standard flame for each of the six filters of the SME 640 camera. The intensity has a periodic oscillation (flickering) whose amplitude should be ideally constant for each point of the flame, but the measured value has small irregularities due to

noise. To determine their value, the envelope of the measured radiance values at one pixel near the burner has been obtained for a time interval of 1 s, and the standard deviation of the radiance values above and below this envelope has been used as the value for  $\Delta\mathcal{L}_i$ . The result was similar for all filters, being  $\Delta\mathcal{L} \sim 5W/m^2 \cdot sr$ . This value was used in a Montecarlo simulation with 100.000 samples to obtain the corresponding distributions of  $\Delta T$  and  $\Delta Q$  using eq. (7). The standard deviations of these distributions furnish the estimation of uncertainties in T and Q.

Tables 1 and 2 show  $\Delta T$  and  $\Delta Q$  for all the possible pairs of filters assuming the radiance of a flame at  $T = 2000$  K and with  $Q = 3000$  ppm·m. Values of uncertainties vary greatly among the different pairs of filters, as expected because of the reasons explained in the previous sub-section.

$\Delta T$	F2	F3	F4	F5	F6
F1	23	47	26	29	36
F2		17	144	15	19
F3			19	52	50
F4				16	21
F5					88

Table 1: Uncertainties in T (measured in K) for different pairs of filters, assuming  $\Delta\mathcal{L}_i = 5 W/m^2 \cdot sr$ , for  $T = 2000$  K;  $Q = 3000$  ppm·m.

$\Delta Q$	F2	F3	F4	F5	F6
F1	88	133	99	78	112
F2		53	820	49	94
F3			57	123	126
F4				51	96
F5					161

Table 2: Uncertainties in Q (measured in ppm·m) for different pairs of filters, assuming  $\Delta\mathcal{L}_i = 5 W/m^2 \cdot sr$ , for  $T = 2000$  K;  $Q = 3000$  ppm·m.

Errors should be reduced if the information of all filters is used. In this case, instead of the system of one equation with one unknown of eq. (6), we have an overdetermined system of six equations with two unknowns,  $\Delta T$  and  $\Delta Q$ . It can be solved using Singular Value Decomposition, which finds an optimal solution in the least-square sense.<sup>6</sup> For  $T = 2000$  K and  $Q = 3000$  ppm·m, the expected uncertainties thus found are  $\Delta T = 11$  K and  $\Delta Q = 35$  ppm·m, smaller, as expected, than the results obtained with any pair of filters.

These uncertainties can be calculated for the whole range of T and Q. Figure 5 shows the results as a contour line plot. It can be observed that uncertainties have a strong variation as a function of the (T,Q) values of the flame. The RMS values obtained for the whole graph are  $\Delta T = 40$  K and  $\Delta Q = 91$  ppm·m.

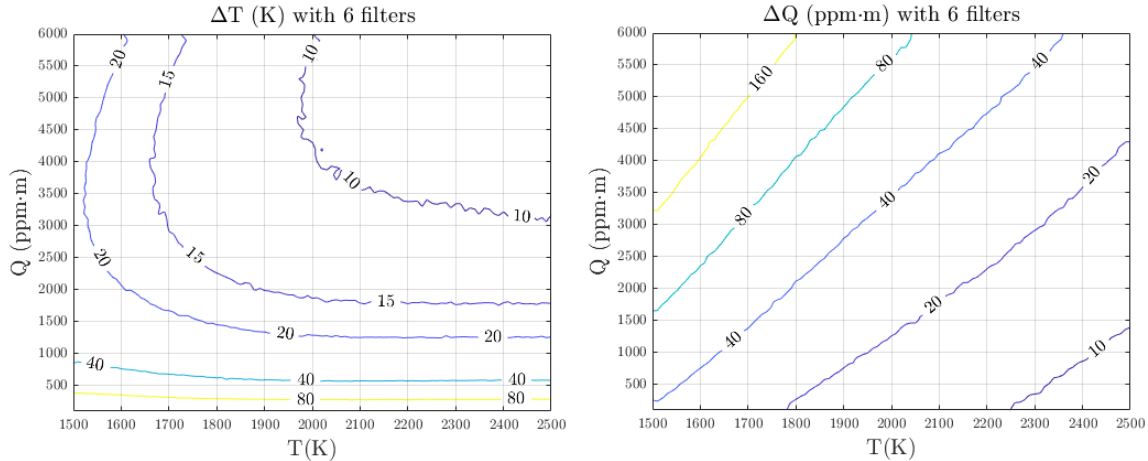


Figure 5: Left: Contour plot of  $\Delta T$  obtained from 6 filters, for different values of  $T$  and  $Q$ . Right: Analogous curves for  $\Delta Q$ . In both cases, uncertainties of  $\Delta \mathcal{L}_i = 5 \text{ W/m}^2\text{-sr}$  have been assigned to each filter.

The main conclusion of this section is that the expected error in both  $T$  and  $Q$  due only to uncertainties in radiance is theoretically quite small and so the multispectral method is in principle feasible. However, real errors may reflect several other factors, and can only be assessed realistically by performing measurements in a real flame. This is the subject of the next section.

## 5. EXPERIMENTAL MEASUREMENTS

To properly test the multispectral measurement method described so far, it is necessary to have a flame whose temperature and  $\text{CO}_2$  column density are well known. This is a demanding requisite, but, as explained in the introduction, is fulfilled by the standard portable flame developed by NPL in the framework of the EMPRESS project.<sup>7</sup> The burner produces a square array ( $40 \times 40 \text{ mm}$ ) of small diffusion flamelets stabilized above it, with a zone of nearly uniform temperature and composition (Figure 6). It uses propane as fuel and can be set to different mixing ratios, from  $\phi = 0,8$  (lean flame) to  $\phi = 1,4$  (rich flame). Temperature, species concentration, and flame dynamics vary with the mixing ratio. A stoichiometric flame  $\phi = 1$  has been used in this work because is the hottest and more stable, and it generates a very small amount of  $\text{CO}$  (hyperspectral measurements retrieved  $Q_{\text{CO}} < 500 \text{ ppm-m}$ , vs.  $Q_{\text{CO}_2} \approx 3500 \text{ ppm-m}$  for points at 20 mm above the surface burner<sup>2</sup>). An additional feature of the standard flame is that the temperature and species concentration spatial profiles are very flat, and therefore the assumption of uniform temperature and concentration along the line of sight is fully justified.



Figure 6: Standard flame burner.

To ensure stability, the flame was turned on, with a mixing ratio  $\phi = 1$ , for one hour before the measurements were performed. The doors and windows of the room remained closed throughout the process to keep temperature

stable and avoid drafts that could cause movements in the flame. A gradual increase in the ambient concentration of CO<sub>2</sub> was observed due to the continuous operation of the flame and the presence of two people in the room, rising from ≈600 ppm before the experiment to ≈1050 ppm at the end.

To retrieve the T and Q values from the multispectral sequence, simulated measurement vectors were previously calculated for temperatures between 1000 and 2500 K and for CO<sub>2</sub> column densities between 1000 and 4000 ppm·m. On the basis of the expected errors determined in Section 4, steps of, respectively, 10 K and 40 ppm·m were used. To keep the processing stage as simple as possible, an average concentration of 850 ppm of ambient CO<sub>2</sub> was used in the calculations.

After selecting a region of interest, the experimental flame images have a size of 260×115 pixels. For each of them, the experimental normalized measurement vector was compared exhaustively with the full set of the simulated ones, and the T,Q couple that returned the best match was assigned to it. This method is computationally expensive but yet affordable for the size of the data handled, and ensures the lowest error solution, unlike a search algorithm which could end up in a local minimum. The discrepancy between experimental and theoretical normalized measurement vectors was quantified as the sum of absolute errors (SAE), defined as  $SAE = \sum_{i=1}^6 |\mathcal{L}_{exp,i} - \mathcal{L}_{sim,i}|$ , instead of the sum of squared errors (SSE) in order not to weight excessively errors of a single filter.

To validate the multispectral temperature and column density maps obtained by this method, they can be compared to those provided by the fitting of hyperspectral images,<sup>2</sup> since hyperspectral temperature profiles in the NPL standard flames have shown a very good agreement (within 1% in K) with the measurements via the Rayleigh scattering thermometry technique, traceable to ITS-90. Although hyperspectral measurements were made on a different day, a comparison is justified because the reproducibility of temperature and species concentration of the flame is extremely good. This is done in Figures 7 and 8. It can be seen that results are qualitatively very similar.

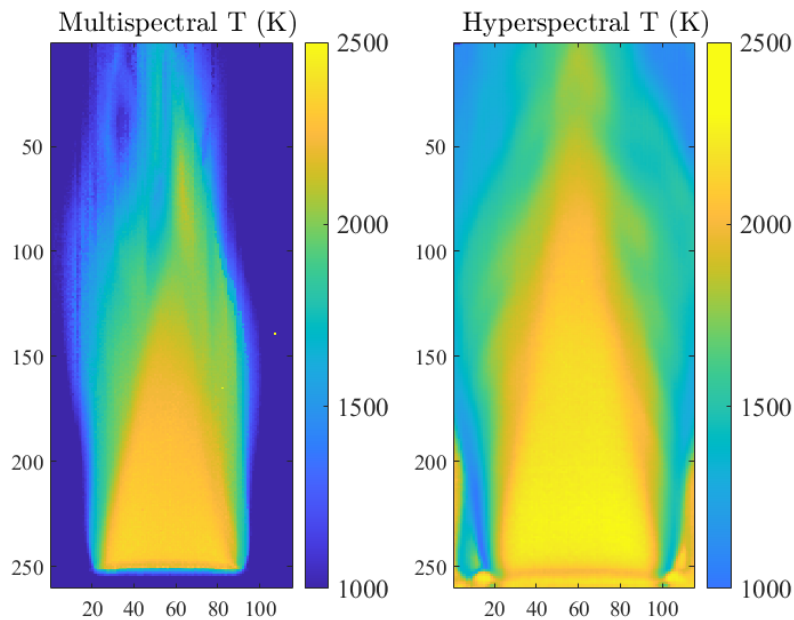


Figure 7: Left: T (K) calculated from multispectral images, by exhaustive search of the least SAE between simulated and experimental normalized measurement vectors. Right: T calculated from hyperspectral images. Scales at the left and bottom of the images show pixel numbers.

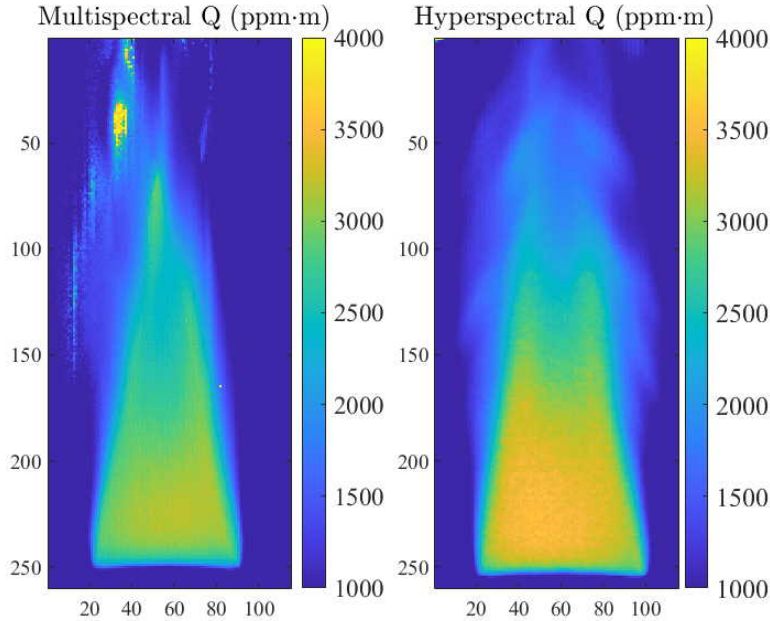


Figure 8: Left:  $Q$  (ppm·m) calculated from multispectral images, by exhaustive search of the least SAE between simulated and experimental normalized measurement vectors. Right:  $Q$  calculated from hyperspectral images. Scales at the left and bottom of the images show pixel numbers.

A more quantitative comparison can be made by studying horizontal profiles of  $T$  and  $Q$  in the flame. For the region near the burner, these should be fairly flat; especially the temperature. Figure 9 shows two pairs of profiles for comparison. Results are unreliable outside the central zone (i.e., approximately for pixels up to No. 20 and from 95 onwards), because radiance, and consequently signal-to-noise ratio, decrease sharply outside of the burner area, which translates into erroneous estimates of  $T$  and  $Q$  for both multispectral and hyperspectral measurements. Also, profiles are not perfectly aligned spatially, due to co-registration errors between the multispectral and hyperspectral images (both instruments have different fields of view and the viewing angle was slightly different). However, the central region, between pixels 30 and 80, is flat in both profiles and makes possible a meaningful comparison.

It is found that the multispectral images have a systematic error, attributing to the flame temperatures too high and column densities too low: they display, on average, a temperature 100 K higher and a  $\text{CO}_2$  column density 400 ppm·m lower than the real ones. This is a much higher error than expected, based on the estimates in Section 4. Since the same amount of signal at any specific wavenumber can be achieved with a lower value  $T$  and a larger value of  $Q$ , it seems that presently the multispectral algorithm is compensating a retrieved  $Q$  too small with a retrieved  $T$  too large. However, the error in  $T$  can be considered yet a good result since, over a value of  $T=2250$  K, it amounts to  $\approx 4.5\%$ , the same order of magnitude of other optical methods which are much more expensive and complex to install and operate.

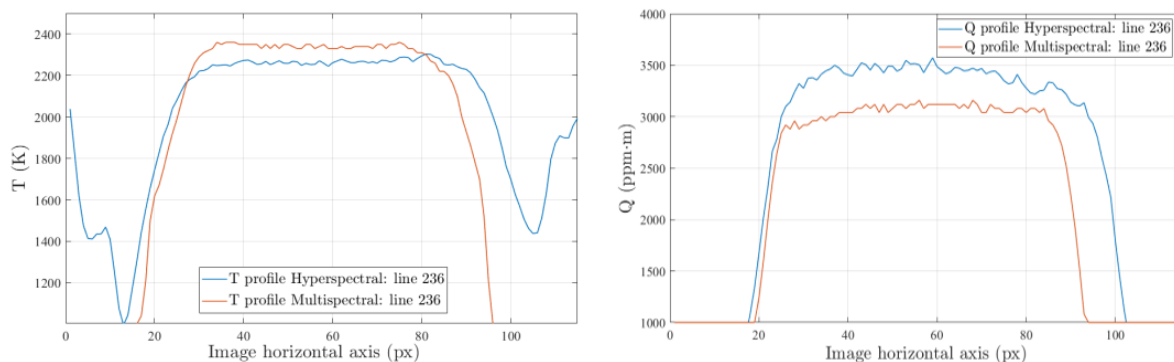


Figure 9: Horizontal profiles at approximately 20 mm above the burner surface (line 236 of Figure 7): left, T; right, Q.

## 6. SUMMARY AND CONCLUSIONS

A multispectral imaging system in the mid-IR region, with six bandpass interference filters, has been setup, radiometrically calibrated, and used to measure temperature (T) and CO<sub>2</sub> column density (Q) of a standard flame of well-known temperature and composition, which had been previously measured by Rayleigh scattering thermometry and emission spectroscopy using hyperspectral imaging. Retrieval of T and Q begins with the simulation of emission spectra as a function of T and Q values, using spectral parameters from the HITEMP2010 database. Simulated spectra are integrated over the spectral bands of the filters, and the results are compared to experimental measurements of the flame with the multispectral system. Values of T and Q are obtained as those that provide the better agreement between simulation and measurements. The proposed method provides maps of T and Q which are in a very good qualitative agreement with those obtained with hyperspectral measurements. Errors in T are  $\approx 4.5\%$ , comparable to those of more expensive and complex optical techniques.

The present work can be developed along several possible lines of future work. The method has been only tested in a very specific flame because it has unique advantages for validation, but to demonstrate its general applicability it should be applied to flames of different characteristics. A starting point will be to use different mixing ratios in the standard flame; in particular rich flames, which have larger amounts of CO, but also flames with non-flat profiles of T and Q, where multispectral results could be tested against those obtained with hyperspectral processing. This study could be also helpful to understand better the sources of error. One point of interest is to test the ability of the method to quantify CO, which would be a very useful feature for the optimization of combustion in industrial applications.

Additional work is needed also to improve accuracy, since real errors have been found to be much larger than those expected from the estimation of Section 4. One possible improvement is to refine the calibration of the multispectral system with the consideration of the spectral profiles of the filters. Although calibration based only on the spectral width works very well with solid targets, the strong spectral structure of flame emission can induce errors that should be studied.

Calibration has to be reconsidered also regarding the values of radiance used. Since the maximum temperature of the blackbody used was 600°C, the calibration had to be extrapolated linearly to the high-radiance range. Although the behavior of the detectors should be linear within their dynamic range, this extrapolation can magnify uncertainties precisely at the signal levels needed for flame measurements at the wavenumbers of peak radiance.

Another area of improvement is the optimization of interference filters. The present set was selected among the band-pass filters available in the laboratory, with the requirement that they had to cover the whole emission band of CO<sub>2</sub> with some degree of overlapping; but it is possible to optimize the spectral profiles to provide a maximum of spectral information and sensitivity to temperature. However, custom-made interference filters are expensive, and the optimal set may depend on the characteristics of the flame, so the benefits of this alternative should be weighted against cost.

Finally, from a practical point of view, our study suggests that although uncertainties increase if the number of channels is reduced, it is yet possible to retrieve temperature from the information of only two filters, with an accuracy that may be good enough for many applications. Therefore, a simple mid-IR bi-spectral system could be a good practical alternative, and it would be an interesting development to pursue.

## ACKNOWLEDGMENTS

The authors would like to acknowledge the financial support from EURAMET through 17IND04 EMPRESS 2 project. This project has received funding from the EMPIR programme co-financed by the Participating States and from the European Union's Horizon 2020 research and innovation programme. This work has been supported also by Comunidad de Madrid (Spain) - Multiannual agreement with UC3M ("Excelencia para el Profesorado Universitario" - EPUC3M14) - Fifth regional research plan 2016-2020. Thanks also to Gavin Sutton and Alberto Sposito for their support in setting up the NPL standard flame at the LIR-Infrared Laboratory at Universidad Carlos III de Madrid.

## REFERENCES

1. J. V. Pearce, F. Edler, C. J. Elliott, L. Rosso, G. Sutton, A. Andreu, and G. Machin, "EMPRESS: A European Project to Enhance Process Control Through Improved Temperature Measurement," *International Journal of Thermophysics* **38**, p. 118, Aug. 2017.
2. G. Sutton, A. Fateev, M. A. Rodríguez-Conejo, J. Meléndez, and G. Guarnizo, "Validation of Emission Spectroscopy Gas Temperature Measurements Using a Standard Flame Traceable to the International Temperature Scale of 1990 (ITS-90)," *International Journal of Thermophysics* **40**, p. 99, Nov. 2019.
3. M. Chamberland, V. Farley, A. Vallières, A. Villemaire, L. Belhumeur, J. Giroux, and J.-F. Legault, "High-performance field-portable imaging radiometric spectrometer technology for hyperspectral imaging applications," in *Chemical and Biological Sensors for Industrial and Environmental Security*, **5994**, p. 59940N, International Society for Optics and Photonics, 2005.
4. "Empress 2 project," 2020. <https://www.strath.ac.uk/research/advancedformingresearchcentre/whatwedo/collaborativeprojects/empress2project/>.
5. L. Rothman, I. Gordon, R. Barber, H. Dothe, R. Gamache, A. Goldman, V. Perevalov, S. Tashkun, and J. Tennyson, "Hitemp, the high-temperature molecular spectroscopic database," *Journal of Quantitative Spectroscopy and Radiative Transfer* **111**(15), pp. 2139–2150, 2010.
6. W. H. Press, H. William, S. A. Teukolsky, A. Saul, W. T. Vetterling, and B. P. Flannery, *Numerical recipes 3rd edition: The art of scientific computing*, Cambridge university press, 2007.
7. G. Sutton, A. Greenen, L. Stanger, and M. de Podesta, "The npl portable standard flame: characterisation of the temperature field above the burner using precision rayleigh scattering thermometry," 2018.